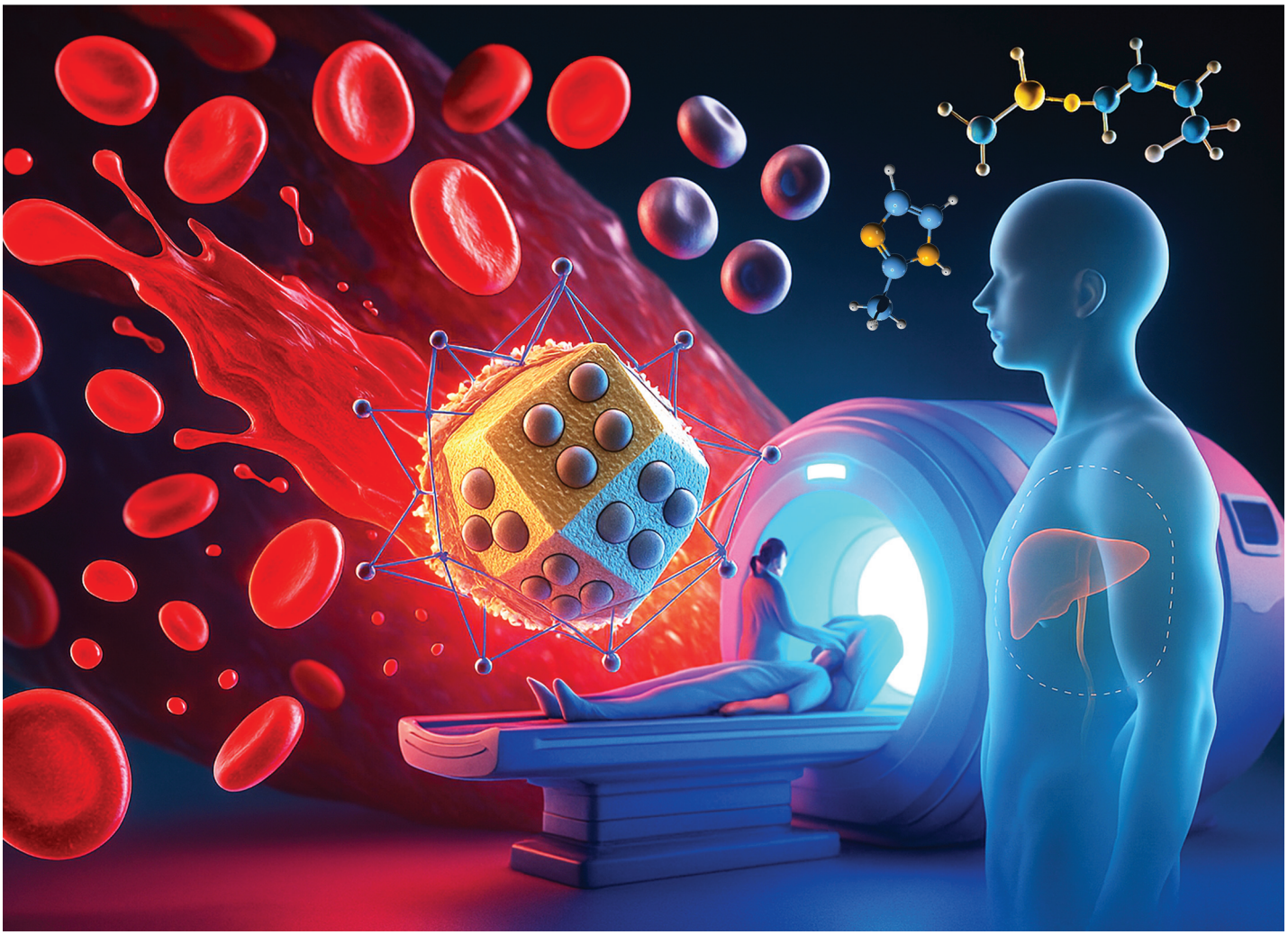

Showcasing research from Dr. Ming-Hsien Chan's Nuclear Medicine and Nanomaterials Laboratory, National Yang Ming Chiao Tung University, Taiwan.

Biomimetic red blood cell membrane-coated FePt metal–organic framework nanoparticles: a multifunctional theranostic system for enhanced MRI and targeted therapy

Magnetic Resonance Imaging (MRI) offers high-resolution visualization of hepatocellular carcinoma (HCC). Conventional iron–platinum nanoparticles (FePt NPs) provide strong *T*2-weighted contrast but are rapidly cleared by macrophages, limiting *in vivo* accumulation. Encapsulation within metal-organic frameworks improves stability and contrast, while red blood cell membrane coating enables immune evasion and tumor targeting. These biomimetic nanocomposites facilitate real-time tracking, sensitive detection, and enhanced monitoring of HCC progression.

Image reproduced by permission of Michael Hsiao and Ming-Hsien Chan from *Nanoscale*, 2025, **17**, 23343.

As featured in:

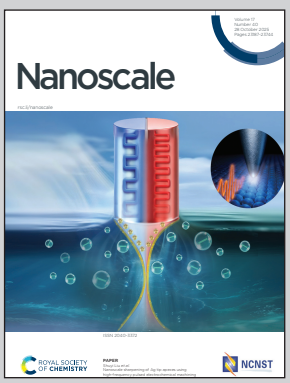

See Ming-Hsien Chan *et al.*, *Nanoscale*, 2025, **17**, 23343.

ROYAL SOCIETY OF CHEMISTRY

rsc.li/nanoscale

Registered charity number: 207890

Nanoscale

PAPER

View Article Online
View Journal | View Issue

Cite this: *Nanoscale*, 2025, **17**, 23343

Biomimetic red blood cell membrane-coated FePt metal–organic framework nanoparticles: a multifunctional theranostic system for enhanced MRI and targeted therapy

Ming-Hsien Chan, *[a] Ru-En Zhuang,[b] Da-Hua Wei *[b] and Michael Hsiao [c,d]

Received 4th August 2025,
Accepted 26th August 2025

DOI: 10.1039/d5nr03294f

rsc.li/nanoscale

Magnetic Resonance Imaging (MRI) is a non-invasive technique that provides high-resolution tissue imaging, making it a potential tool for hepatocellular carcinoma (HCC) imaging diagnosis. However, effective visualization of HCC-related molecular changes requires advanced nanoscale contrast agents with surface modifications for specific biomarker binding. Iron-platinum nanoparticles (FePt NPs) are widely used for *T*2-weighted MRI contrast but are rapidly degraded by macrophages, limiting their accumulation and signal enhancement *in vivo*. To address this issue, metal–organic frameworks (MOFs) can encapsulate FePt NPs to improve stability and imaging contrast. Additionally, red blood cell membrane (RBC-m) coating enhances tumor tissue accumulation, enabling real-time tracking and diagnosis of HCC. Initial studies have demonstrated the effectiveness of this technology in HCC imaging diagnosis, contributing to disease monitoring and treatment evaluation. With further optimization, these nanocomposite probes have the potential to enhance MRI-based HCC diagnostics, bridging molecular biology and clinical imaging to advance personalized medicine.

Introduction

Hepatocellular carcinoma (HCC) is the most common primary liver cancer, accounting for the majority of liver cancer cases worldwide.[1] It typically arises in the context of chronic liver diseases such as hepatitis B or C virus infection, alcohol-related liver damage, or non-alcoholic fatty liver disease (NAFLD).[2] HCC is a leading cause of liver cancer-related mortality, characterized by aggressive tumor growth, vascular invasion, and a high rate of recurrence following treatment. Early and accurate diagnosis of HCC is crucial, as it significantly improves treatment outcomes and patient survival.[3] As a non-invasive tomographic imaging technique, magnetic resonance imaging (MRI) offers higher spatial resolution than common fluorescence or ultrasonic imaging.[4] Its ability to penetrate tissues deeply has led to widespread applications in biological research and disease diagnosis. In MRI, proton imaging and contrast agents (CAs) are commonly employed to enhance imaging performance and improve the signal-to-noise ratio (SNR).[5] *T*2-type CAs, exemplified by superparamagnetic iron oxide nanoparticles (SPIONs) or other iron-based nanoparticles such as superparamagnetic iron-platinum nanoparticles (FePt NPs), and *T*1-type CAs, represented by Gd^{3+} and Mn^{2+}, are widely used.[6] While *T*2-type CAs exhibit excellent biocompatibility, their specific diffusion effects (resulting in blurred imaging edges) limit their analytical capabilities. In contrast, *T*1-type CAs are favored in analytical and detection applications due to their broader applicability and more distinct imaging signals.[7]

However, *T*1-type CAs often exhibit high nephrotoxicity, raising concerns about their use. Developing new CAs that adapt to complex biological environments is critical for enhancing MRI performance and expanding its applications in disease diagnosis. Retaining the biocompatibility of ultra-small iron-based NPs has demonstrated exceptional *T*1-CA capabilities and is extensively used in biomedical detection.[8] Their smaller size reduces the volume magnetic anisotropy and spin disorder, significantly decreasing their magnetic moments.[9] FePt NPs, with a size of around 5–10 nm, exhibit *T*1 imaging performance.[10] However, as their size increases due to aggregation or assembly, their excellent *T*2 imaging capability is enhanced, enabling FePt NPs to revert to their original *T*2 imaging capabilities.[11] This *T*1-to-*T*2 imaging conversion provides opportunities to design unique, targeted probes for

[a]*Department of Biomedical Imaging and Radiological Sciences, National Yang Ming Chiao Tung University, Taipei 112, Taiwan. E-mail: mhchan@nycu.edu.tw*
[b]*Graduate Institute of Manufacturing Technology and Department of Mechanical Engineering, National Taipei University of Technology, Taipei 106, Taiwan. E-mail: dhwei@ntut.edu.tw*
[c]*Genomics Research Center, Academia Sinica, Taipei 115, Taiwan*
[d]*Department and Graduate Institute of Veterinary Medicine, School of Veterinary Medicine, National Taiwan University, Taipei 116, Taiwan*

detecting lesions in specific areas such as the liver, brain, tumors, or other sites. These probes aim to achieve improved *T*1-to-*T*2 or *T*2-to-*T*1 imaging for diagnostic purposes.[12] The natural glycans, proteins, and lipids on RBC membranes allow the coated NPs to mimic native cells, increasing their blood circulation time and improving their biodistribution.[13] RBC membranes can be functionalized to carry specific ligands or antibodies, enabling the NPs to sense molecules and target particular tissues or tumor environments.

Organic nucleotides or antibodies can be further modified through the RBC membrane, and these biosensing molecules can be used to detect biomarkers.[27] By disguising the NPs as RBCs, the coating minimizes unintended interactions with healthy tissues,[27] enhancing the therapeutic index of the loaded drugs or diagnostic agents. However, it is not easy to coat biofilms on inorganic materials.[28] Even if the material can be coated, the biofilm will easily fall off or cause the nanomaterials to deteriorate. Therefore, according to previous research, the use of metal–organic frameworks (MOFs) can effectively serve as a mediator between inorganic materials and organic biofilms.[29] MOFs consist of inorganic metal nodes (*e.g.*, metal ions or clusters) and organic linkers, such as carboxylates, amines, or phosphonates.[30] This combination inherently bridges the inorganic and organic domains, enabling synergistic interactions between the two. The structure of MOFs can be finely tuned by varying the choice of metal centers and organic linkers.[31] This customization allows MOFs to adapt their chemical, mechanical, and electronic properties to specific applications, making them versatile mediators between inorganic and organic systems.[32] Moreover, MOFs can be designed to possess functional groups on their surfaces that are chemically compatible with organic and inorganic components.[33] For instance, their organic linkers can interact with biological molecules, while the metal centers can coordinate with inorganic species. In 2023, the research team led by Dr Romy Ettlinger developed Fe_3O_4-ZIF-8 NPs and proposed their potential application in theranostics for cancer treatment.[34] This research focuses on utilizing metal–organic frameworks to encapsulate iron ions as imaging agents.[35] The metal–organic framework (MOF), like ZIF-8 (zeolitic imidazolate framework-8), serves as a vehicle, while the Fe_3O_4 core embedded within the MOF allows visualization through magnetic resonance imaging (MRI).[36] In addition, MOFs are known for their exceptionally high surface areas and porous structures. These features provide ample space for interactions at the inorganic–organic interface, which are highly suitable for MRI applications.[37] Except for MOFs and RBC membranes, there are many other modification strategies to enhance circulation time, biocompatibility, and imaging persistence. These approaches are summarized in Table 1. MOFs possess pH- or

Table 1 Representative magnetic nanoparticles and nanocomposites for MRI applications, their imaging modes, biodegradability/biopersistence characteristics, and selected references

Category	Representative materials	MRI mode	Biodegradability/biopersistence	Ref.
IONPs (control)	SPIONs, ES-MIONs	*T*2	Well-documented metabolism *via* iron pathways; relatively predictable clearance. However, rapid RES uptake can lead to fast signal loss	14 and 15
Nanoalloys (control, this work)	FePt, FeMn	Mainly *T*2 (dual-modal possible)	Alloy cores are chemically stable, supporting strong contrast. However, slow or incomplete degradation may cause long-term retention and potential metal toxicity, making biosafety less predictable than biodegradable systems	16 and 17
MOFs (this work)	ZIF-8, MIL-100(Fe), MIL-88A (Fe)	*T*1/*T*2 or multimodal	Exhibit pH- or phosphate-responsive degradation. Their highly tunable structures and responsive behavior make them particularly attractive for tumor-targeted therapy and imaging	18 and 19
Membrane cloaking (this work)	RBC membrane	—	Reduce immune clearance and mitigate long-term accumulation toxicity compared to uncoated nanoparticles	20
Graphitic carbon shell	FeCo@C, Fe@C (graphitic/diamond-like carbon shells)	*T*2	Carbon shells are chemically inert and protect the core; high colloidal and *in vivo* stability associated with prolonged biopersistence	21
Silica encapsulation	SPION@SiO_2	*T*2	Silica shells (especially dense) slow dissolution and ion release; PEGylation further reduces clearance, supporting long-term stability	22
Zwitterionic stealth polymers	Poly(carboxybetaine), carboxybetaine-based membranes	*T*2 (platform-agnostic)	Ultra-low fouling surfaces yield ultra-long blood circulation ($t1/2$ up to ~96 h reported), sustaining blood-pool MRI and delaying RES uptake	23
Albumin cloaking	HSA-coated SPIONs	*T*2 (sometimes *T*1/*T*2*)	Endogenous-protein camouflage increases biocompatibility and extends circulation; slower RES clearance than bare SPIONs	24
Cobalt ferrite ferrites	$CoFe_2O_4$ (SPM or ferrimagnetic, size-dependent)	*T*2	Higher chemical stability and lower biodegradation than magnetite; reports of long-term retention with slow biological remediation (*e.g.*, *via* ferritin)	25
Prussian blue frameworks	Prussian blue nanoparticles (PBNPs), PB-coated ferrites	Primarily *T*1 (can be *T*2 or dual with ferrites)	Chemically stable iron hexacyanoferrate network; good *in vivo* stability and slow degradation, enabling a persistent signal	26

phosphate-responsive degradability and tunable structures, making them particularly advantageous for tumor-targeted therapy and imaging. Other strategies, such as membrane coating, can further improve circulation time.

Magnetic hyperthermia (MFH) is an emerging cancer treatment modality that utilizes magnetic nanoparticles to generate localized heat upon exposure to an alternating magnetic field (AMF). This heat induces tumor cell apoptosis or sensitizes cells to chemotherapeutic agents, without significantly affecting surrounding healthy tissues. Among various magnetic materials, FePt nanoparticles are particularly attractive due to their high magnetic anisotropy, thermal stability, and strong heating efficiency under an AMF. When combined with drug delivery systems or biological coatings such as red blood cell membranes, MFH not only offers precise tumor targeting but also enables synergistic therapeutic outcomes by integrating thermal ablation with chemotherapy. Therefore, engineering nanoplatforms that can achieve both MFH and drug delivery holds great promise for enhanced anticancer efficacy.

This study attempts to develop (1) FePt clusters within MOFs for *T*2 contrast enhancement, (2) a multifunctional therapeutic modality (drug delivery + hyperthermia), and (3) RBC membrane (RBC-m) cloaking for immune evasion. Such a multi-strategy platform is rarely reported and exhibits promising *in vivo* performance in MRI and therapeutic efficacy, as evidenced by our biodistribution, imaging, and tumor suppression data. RBC-m has been combined to synthesize magnetic nanocomposites, FePt@ZIF-m, with long-lasting MRI diagnosis. Furthermore, the novel FePt@ZIF-m system is not only used for MRI diagnosis but also for enhancing its therapeutic efficacy against HCC.[38] We attempt to integrate the magnetic hyperthermia (MHT) effect of FePt NPs, allowing it to induce localized heating in the tumor region through an external magnetic field while simultaneously serving as an MRI diagnostic agent, thereby killing cancer cells. The development of this dual-functional "imaging diagnosis-hyperthermia therapy" probe will contribute to improving the early diagnosis rate of HCC and providing more effective personalized treatment strategies.

Results and discussion

By leveraging natural RBC membranes, we try to overcome the limitations of FePt NPs and MOFs, such as their short half-life in the bloodstream and lack of cancer-targeting capabilities. By encapsulating FePt@ZIF-8 within the RBC-m, we can generate FePt@ZIF-m nanocomposites to take advantage of the stealth properties of the membrane to help NPs evade immune detection and clearance *in vivo* (Fig. 1a). Furthermore, this strategy allows us to utilize specific proteins and receptors on the membrane to achieve targeted delivery to specific tissues or cells, thereby enhancing therapeutic efficacy and reducing damage to surrounding healthy tissues. Multifunctional nanocomposite materials have consistently been a key research focus worldwide, with a significant increase in related studies and publications. This research aims to develop highly biocompatible magnetic nanomaterials and excellent magnetic properties. These materials are designed to retain certain magnetic characteristics while prolonging their circulation time in the body, reducing the likelihood of clearance by the immune system.[39] FePt magnetic materials were chosen due to their superior chemical stability compared to widely studied iron-oxide NPs when selecting materials. These particles were synthesized to enhance performance with a zeolitic imidazolate framework (ZIF), which features a high surface area, excellent adsorption properties, good biocompatibility, and suitability as a bridge between organic and inorganic materials. Subsequently, the outer layer of the material was encapsulated with an RBC membrane to increase its circulation time in the bloodstream.

The resulting multifunctional nanocomposite material exhibits high adsorption capacity, magnetic properties, and biocompatibility. Regarding the fundamental properties of various nanomaterials, we can first analyze their crystal structures using X-ray powder diffraction (XRD), as shown in Fig. 1b. The measured data were compared with the standard ZIF-8 spectrum (JCPDS no. 00-062-1030; XRD data not included here, only reference information listed). The characteristic peaks of ZIF-8 were observed at 10.4° (002), 12.7° (112), 14.7° (022), 16.4° (013), 18° (222), and 29.6° (044).[40] The sharp and narrow full width at half maximum (FWHM) peaks indicate good crystallinity. These data mainly reflect the crystal structure of FePt@ZIF nanocomposite materials with different proportions of ZIF-8 added. Diffraction peaks of ZIF-8 can also be observed and are assigned to the corresponding crystallographic planes. It was found that the intensity of the diffraction peaks increased with the addition of ZIF-8. Comparing the measurement data with the FePt standard spectrum (JCPDS no. 29-0717), a diffraction peak corresponding to the (111) plane of FePt NPs was observed at 40.3°. However, the strong signals from ZIF-8 suppressed the original FePt signals. Using transmission electron microscopy (TEM) and scanning electron microscopy (SEM), we examined the particle size, distribution, and surface morphology of FePt (Fig. 1c), ZIF-8 (Fig. 1d), and FePt@ZIF (Fig. 1e). Elemental analysis of these materials was performed using energy-dispersive X-ray spectroscopy (EDX). In the TEM images, FePt NPs appeared as agglomerated spherical structures. SEM images further revealed that the FePt NPs aggregated into clusters with an average particle size of approximately 13.65 nm. Additionally, EDX analysis showed a very pure distribution of Fe and Pt elements.

For ZIF-8 particles, the TEM images displayed uniform hexagonal shapes with an average particle size of about 97.57 nm. Due to the direct deposition of powdered particles onto a carbon film during SEM sample preparation, SEM images showed ZIF-8 particles in an aggregated form. EDX analysis confirmed the presence of zinc ions (Zn^{2+} from Zn elements), carbon, and nitrogen (from the organic ligands) in ZIF-8, with uniform element distribution within the particles. This demonstrates the high purity of the ZIF-8 particles and highlights the potential of their MOF structure to serve as an interface bridging inorganic and organic materials. For the FePt@ZIF nanocomposite material, TEM images showed that

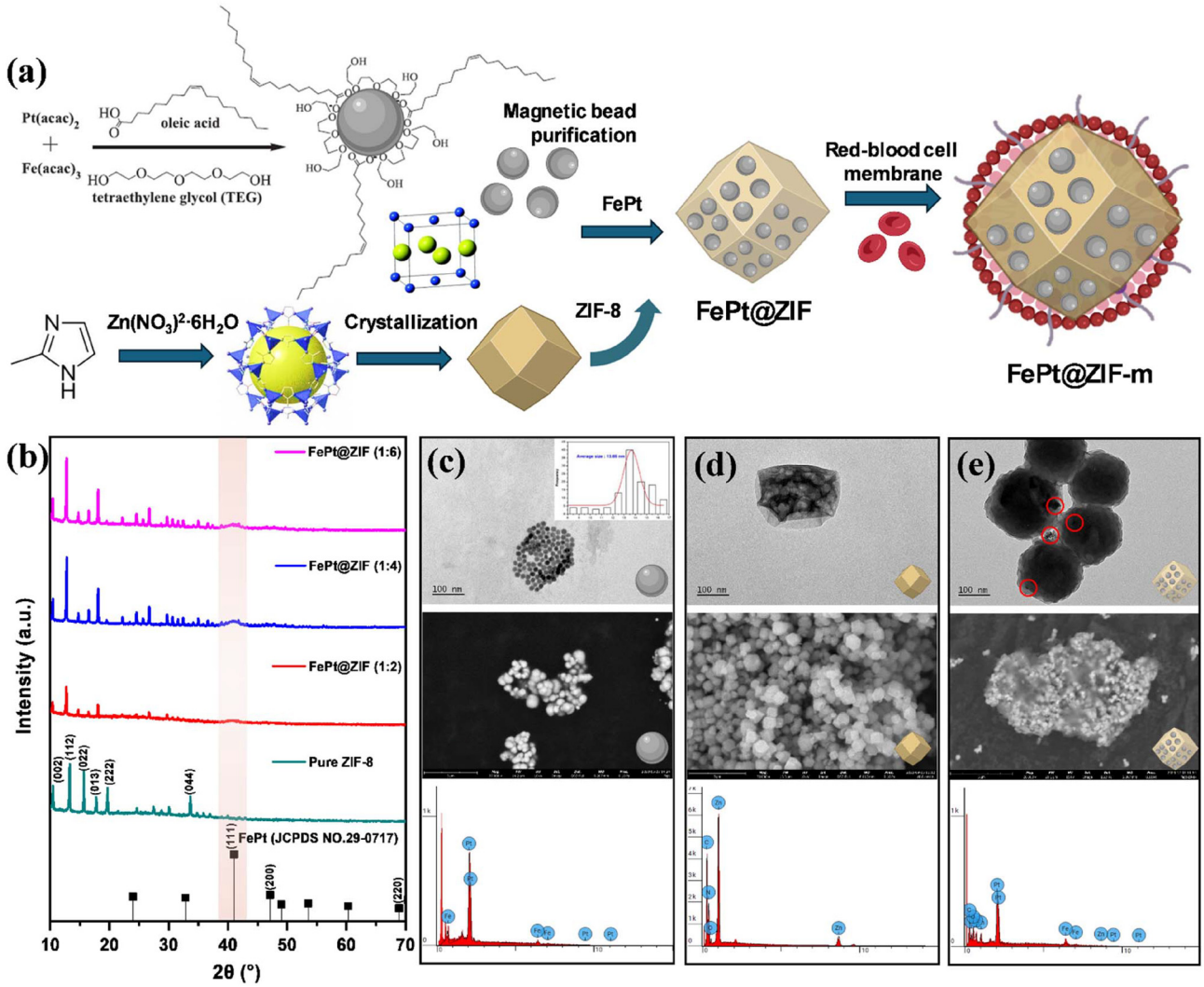

Fig. 1 (a) Schematic diagram of the synthesis of FePt@ZIF-a and FePt@ZIF-m nanomaterials. Analysis of the basic morphology, elements, and crystal structure of FePt, ZIF-8, and FePt@ZIF. (b) XRD patterns for ZIF-8 compared with FePt@ZIF by varying weight ratios. TEM, SEM, and EDX images of (c) FePt, (d) ZIF-8, and (e) FePt@ZIF.

FePt NPs were successfully adsorbed onto both the surface and internal structure of the ZIF-8 particles, leveraging the high porosity of ZIF-8 to load FePt NPs. EDX analysis confirmed the presence of both Fe and Pt elements within the composite particles, proving the successful synthesis of the FePt@ZIF nanocomposite material with elemental mapping measurement (Fig. S1a to S1c). MOFs are characterized by highly tunable pore sizes, ranging from micropores (<2 nm) to mesopores (2–50 nm) and even macropores (>50 nm) in some cases. This tunability is achieved by selecting appropriate organic linkers and metal nodes during synthesis. Therefore, whether ZIF-8 successfully encapsulates FePt NPs can be further analyzed through changes in its porosity. We utilized the Brunauer–Emmett–Teller (BET) surface area analyzer (Fig. S2b) to study the specific surface area and pore size distribution of FePt, ZIF-8, and FePt@ZIF under different pressures (Fig. S2d). The adsorption performance of FePt NPs was poor across low- to high-pressure conditions. Using the BJH equation, the pore size was calculated to be approximately 28.4 nm (since this is larger than the physical size of the nanomaterial, it can be considered a non-porous material), as shown in Fig. S2a.

The pore volume was about 0.046 $cm^3\ g^{-1}$, indicating that the low-porosity FePt NPs exhibit inferior gas adsorption properties (Fig. S2f). ZIF-8 demonstrated excellent gas adsorption performance in both high-pressure and low-pressure environments. In eqn (1), P represents the equilibrium pressure of the adsorbed gas at the adsorption temperature, P_0 is the saturation vapor pressure, C is the adsorption constant of the sample, also known as the BET constant, and V is the equilibrium volume of the adsorbed gas.

$$\frac{P}{V(P_0 - P)} = \frac{1}{V_m \times C} + \frac{C - 1}{V_m \times C} \times \frac{P}{P_0} \quad (1)$$

Using the Barrett–Joyner–Halenda (BJH) equation, its average pore size was calculated to be about 53.5 nm, with a pore volume of approximately 0.731 $cm^3\ g^{-1}$, highlighting its high porosity. Moreover, the specific surface area of ZIF-8 reached as high as 1041.6 $m^2\ g^{-1}$, significantly higher than the 6.2 $m^2\ g^{-1}$ of FePt NPs, proving that ZIF-8 has a sufficient surface area and porosity to encapsulate FePt NPs. Additionally, we compared different ratios of FePt NPs to ZIF-8, but it was evident that the N_2 adsorption isotherms of both ZIF-8 and FePt@ZIF composite materials consistently exhibited type II behavior, indicating the presence of irregular pore structures (Fig. S2e). The stability of the materials was investigated using a thermogravimetric analyzer (TGA) and differential thermal analysis (DTA) to analyze the behavior of FePt, ZIF-8, and FePt@ZIF at different temperatures (Fig. S2c). The testing conditions involved a heating rate of 5 °C per minute, as shown in Fig. S2g to S2i. For FePt, a weight loss of approximately 6% was observed between 100 and 250 °C, likely due to the evaporation of physically adsorbed water molecules. For ZIF-8, a significant weight loss occurred between 400 and 500 °C, indicating the decomposition of organic molecules from 2-methylimidazole. In the case of FePt@ZIF, a weight loss of about 15% was observed between 300 and 350 °C, which may be attributed to the decomposition of guest solvent molecules. Additionally, further weight loss occurred between 350 and 450 °C due to the decomposition of 2-methylimidazole, suggesting a two-step decomposition process in the composite material. The synthesized magnetic FePt@ZIF NPs were coated with an RBC membrane layer to enhance biocompatibility and prolong circulation time in the bloodstream. Since RBC membranes are organic materials and FePt NPs are inorganic, a MOF (ZIF-8) was selected as a bridge to connect these components. In this work, the FePt@ZIF-m composite material was prepared using a physical extrusion method. TEM was employed to observe the surface morphology of FePt@ZIF-m and analyze the synthesis results. It was evident that the FePt@ZIF NPs were successfully encapsulated within the RBC membrane, as shown in Fig. 2a. The FePt@ZIF-m particles exhibited a large spherical morphology with average particle sizes of 175.48 nm, 161.47 nm, and 169.13 nm, respect-

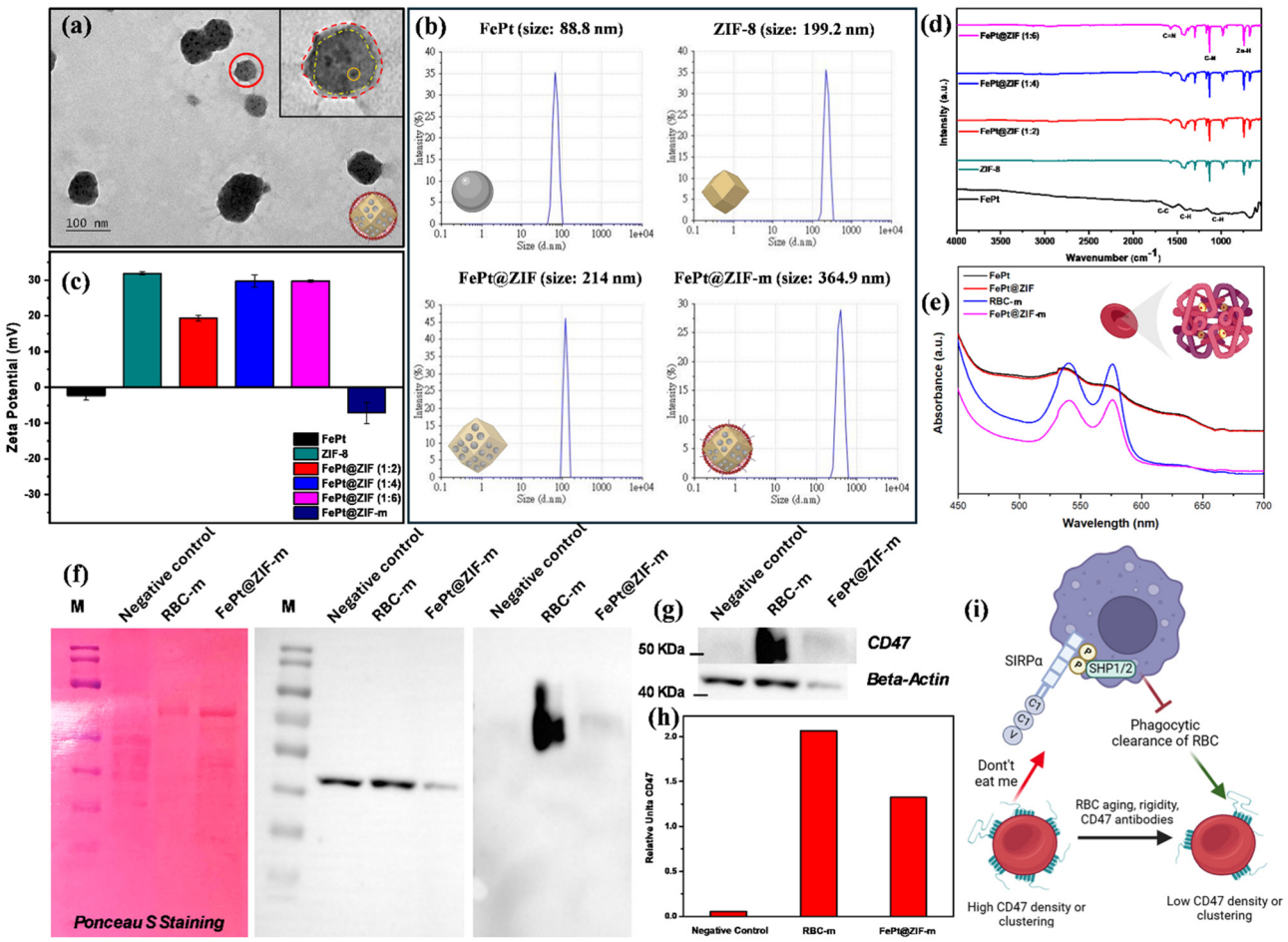

Fig. 2 Qualitative surface analysis of FePt@ZIF and FePt@ZIF-m. (a) TEM image of FePt@ZIF-m. (b) DLS particle size and (c) surface zeta potential analysis of FePt, ZIF-8, FePt@ZIF, and FePt@ZIF-m. (d) FTIR surface functional group detection of FePt, ZIF-8, and FePt@ZIF. (e) UV-Vis detection of the characteristic peak spectrum of hemoglobin in RBC-m. (f) Comparison of Ponceau S and western blot. CD47 (g) western blot and (h) protein quantification results. (i) CD47 plays a role in RBC-m to avoid macrophage phagocytosis.

ively. This demonstrates that the physical extrusion method effectively integrates nanoparticles with RBC membranes, enhancing sample biocompatibility and the potential for *in situ* MRI bio-sensing signal simulation in subsequent experiments. Since the primary research subjects for biosensors often involve small molecules, drugs, or medical materials that come into contact with the human body, safety is of utmost importance. Thus, accurate measurements—such as simulating human environmental conditions like body temperature or high salinity—reflect the behavior of drugs within the human body. Dynamic light scattering (DLS) and zeta potential technology were used to average the hydrodynamic radius under different pH conditions. These were measured to represent the charge density and swelling behavior of polymer functional groups in varying proportions. In Fig. 2b and c, experimental results revealed that the hydrodynamic radius also increased after generating the nanocomposites (from FePt to ZIF-8, FePt@ZIF and FePt@ZIF-m). The zeta potential measurements showed that FePt nanoparticles (NPs) were nearly neutral, with a zeta potential of −2.3 mV, while ZIF-8 exhibited a stable positive zeta potential of 29 mV. When FePt was combined with different weight ratios of ZIF-8 to form the FePt@ZIF composite, the zeta potential shifted to a positive value as the weight of ZIF-8 increased, with a gradual rise in the potential value. Finally, the FePt@ZIF-m composite material coated with an RBC membrane shifted the zeta potential from positive to negative (−7.12 mV) due to the negatively charged RBC membrane. This change indicates that the composite material possesses excellent stability. The surface functional groups of the materials were analyzed using Fourier-transform infrared spectroscopy (FTIR, Fig. 2d). Due to the use of triethylene glycol (TEG) and oleic acid as solvents in synthesizing FePt NPs, TEG's carbon, hydrogen, and oxygen functional groups were observed in the range of 500 to 1700 cm^{-1}. Next, the chemical structure and surface functional groups of ZIF-8 were analyzed. The FTIR spectrum of the synthesized ZIF-8 showed a C=N bond vibration at 1600 cm^{-1}. Vibrations corresponding to C–N bonds were observed in the 995–1145 cm^{-1} range, associated with the imidazole ring in 2-methylimidazole. Peaks appearing in the 900–1350 cm^{-1} range indicated in-plane bending of the imidazole ring. At 690 and 750 cm^{-1}, aromatic C–H bond bending was observed. Additionally, several weak peaks between the major peaks were detected, potentially due to protonated groups formed from water molecule clusters. To evaluate the integration of the RBC membrane (RBC-m) with the material, we employed UV-Vis absorption spectroscopy (Fig. 2e) and western blot analysis (Fig. 2f–h) to examine the hemoglobin spectrum and the presence of Cluster of Differentiation 47 (CD47), also referred to as integrin-associated protein (IAP).[41] These analyses confirmed that FePt@ZIF successfully bonded with RBC-m to form FePt@ZIF-m. Hemoglobin absorption was measured in the range of 450–700 nm. While FePt nanoparticles and FePt@ZIF composites showed no significant difference in background absorption spectra, distinct absorption bands were observed at 540 nm and 575 nm for RBC-m and FePt@ZIF-m, respectively. This indicates that the physical extrusion method effectively combined RBC-m with the FePt@ZIF nanocomposite. CD47, a member of the immunoglobulin superfamily, interacts with membrane integrins and binds to ligands such as thrombospondin-1 (TSP-1) and signal-regulatory protein alpha (SIRPα).[42] Acting as a "don't eat me" signal to immune system macrophages, CD47 has gained attention as a potential therapeutic target in some cancers (Fig. 2i). Due to its high expression on RBC membranes, we performed protein detection analyses of RBC-m and FePt@ZIF-m nanocomposites using Ponceau S staining and western blot.[43]

The Ponceau S results revealed that FePt@ZIF-m and RBC-m contained proteins, displaying patterns distinct from the negative control (normal cell pellet). Western blot analysis quantified the CD47 protein originating from RBC-m, with the signal also detected in FePt@ZIF-m, indicating the successful encapsulation of the FePt@ZIF composite by RBC-m. Quantitative analysis of the CD47 protein further confirmed that RBC-m exhibited the highest relative intensity, followed by FePt@ZIF-m. In contrast, the negative control (pellet) showed the lowest signal, validating the successful construction of FePt@ZIF-m nanocomposites with RBC membrane coating. Thus, it was first necessary to confirm the magnetic properties of the materials. We measured these properties using a vibrating-sample magnetometer (VSM) and *T*2-weighted phantom MRI. VSM analysis of the FePt nanoparticles (NPs) revealed their magnetic properties (Fig. 3a). Measurements were performed at room temperature under an applied magnetic field ranging from +20 000 Oe to −20 000 Oe, showing a saturation magnetization of 15.68 emu g^{-1}. The hysteresis loop indicated paramagnetism. When the particle size decreases to a critical point, the anisotropy of the magnetic core diminishes with the volume, reducing the energy barrier for magnetic moment flipping. The addition of varying weight ratios of ZIF-8 to the synthesized samples maintained the paramagnetic properties but showed a declining trend in saturation magnetization with an increasing ZIF-8 content, measuring 11.38 emu g^{-1}, 9.29 emu g^{-1}, and 7.89 emu g^{-1}, respectively. This reduction is attributed to the non-magnetic nature of ZIF-8, as its soft material properties fail to provide sufficient spatial pressure and stress for FePt nanoparticles, increasing the average distance between particles and reducing magnetic interactions. This phenomenon was corroborated in MRI *T*2-weighted phantom data.

Using a magnetic field strength of 7 T, different sample concentrations were placed in a 1% agarose gel solvent, and the transverse relaxation time (spin–spin relaxation time, *T*2) was measured with an MRI system. The relaxation rate ($1/T2$) was plotted against ion concentration to determine the materials' transverse relaxivity (r^2). Measurements were performed for FePt NPs, ZIF-8, and FePt@ZIF at concentrations of 0.5, 0.25, 0.12, 0.06, and 0.03 mg mL^{-1}. The *T*2-weighted images darkened with increasing FePt and FePt@ZIF nanocomposite concentrations, indicating enhanced contrast imaging with higher concentrations. Conversely, non-magnetic

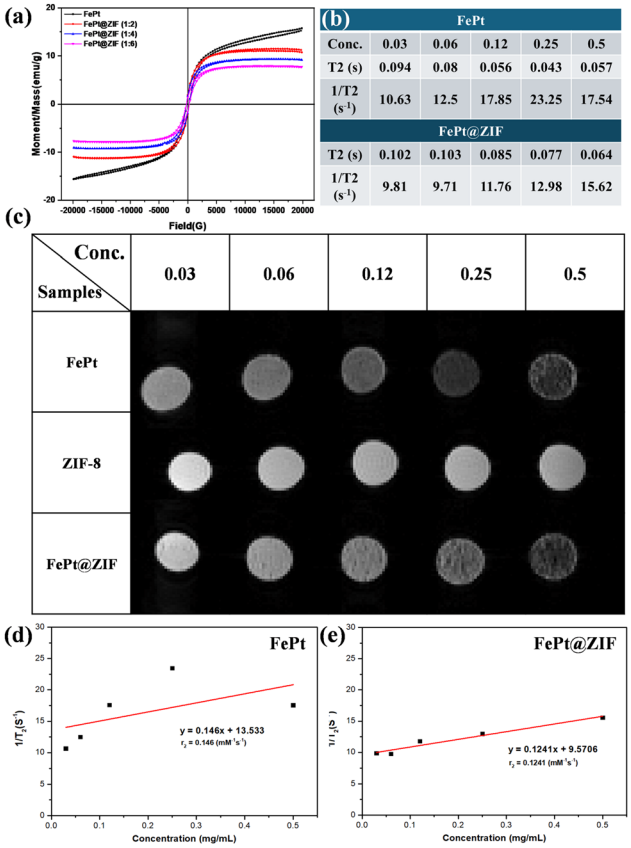

Fig. 3 Analysis of the magnetic properties of FePt NPs, ZIF-8, and FePt@ZIF nanomaterials. (a) The VSM magnetic pattern of FePt@ZIF with different ratios. (b) Quantitative MRI *T*2-weighted phantom data for FePt and FePt@ZIF wearing magnets. (c) MRI *T*2-weighted phantom image. 1/*T*2 linear regression plot of (d) FePt and (e) FePt@ZIF NPs at different concentrations.

ZIF-8 exhibited no significant changes (Fig. 3c). The reciprocal of *T*2 (1/*T*2) was plotted, as shown in Fig. 3b, to obtain quantitative results for FePt and FePt@ZIF NPs. Linear regression of 1/*T*2 yielded an r^2 value of 0.146 mM^{-1} s^{-1}, demonstrating the ability of FePt NPs to shorten the transverse relaxation time, making them effective as MRI contrast agents (Fig. 3d). Compared to FePt NPs, FePt@ZIF NPs exhibited an r^2 value of 0.1241 mM^{-1} s^{-1} (Fig. 3e), likely due to the lower saturation magnetization of FePt@ZIF nanocomposites. While the signal change is less pronounced, FePt@ZIF NPs remain a viable option as MRI contrast agents.

In addition to serving as an MRI contrast agent, FePt@ZIF can also be utilized as a tool for magnetic fluid hyperthermia (MFH) through exposure to a high-frequency magnetic field.[44] MFH is a promising cancer treatment technique that utilizes magnetic nanoparticles to generate localized heat under an alternating magnetic field (AMF). When exposed to an external AMF, these nanoparticles convert electromagnetic energy into heat through Néel and Brownian relaxation processes, leading to a controlled temperature increase. If the temperature reaches 41–45 °C, it can effectively induce apoptosis or necrosis in cancer cells while minimizing damage to surrounding healthy tissues. MFH has been widely studied for its potential in tumor ablation, drug delivery enhancement, and combination therapies with chemotherapy or radiotherapy. Thus, a high-frequency induction heater with an output frequency of 800 kHz and a magnetic field intensity of 3.8 kA m^{-1} was used. The samples were dispersed in DI water at a concentration of 6 mg mL^{-1} for measurement. The magnetic heating data of FePt and FePt@ZIF nanocomposite materials were analyzed. It was observed that FePt nanoparticles exhibited the fastest heating rate, while the heating rate gradually decreased as the proportion of ZIF-8 increased, as shown in Fig. 4b and c. The pure FePt sample reached a temperature above 41 °C—sufficient to kill cancer cells—within 1 minute and 30 seconds, while other samples also reached above 42 °C within 3 minutes. The results showed an inverse relationship with saturation magnetization, confirming that saturation magnetization is correlated with the heating rate. In addition to temperature measurement, thermal imaging can also be used to observe heating variations (Fig. 4d), further confirming that the composite material can be heated under an AMF environment. Next, the heating effect of the prepared magnetic nanocomposite materials was analyzed.

The temperature change was recorded to calculate the slope (representing the temperature rise rate per unit time). Using eqn (2), the specific absorption rate (SAR) of the magnetic nanocomposite materials was calculated, as shown in Fig. 4a. Samples with faster heating rates had larger slope values, indicating that they could reach higher temperatures in the same period

$$\mathrm{SAR} = C\left(\frac{\Delta T}{\Delta t}\right)\frac{1}{m_{\mathrm{FePt}}}. \quad (2)$$

(a)

Samples	m_{Sample} (g)	m_{Water} (L)	M_s (emu/g)	$\Delta T/\Delta t$ (°C/s)	SAR(W/g)
FePt NPs	6×10^{-3}	1×10^{-3}	15.68	0.141	97.67
FePt@ZIF (1:2)	6×10^{-3}	1×10^{-3}	11.38	0.0944	65.39
FePt@ZIF (1:4)	6×10^{-3}	1×10^{-3}	9.29	0.0902	62.48
FePt@ZIF (1:6)	6×10^{-3}	1×10^{-3}	7.89	0.0638	44.19

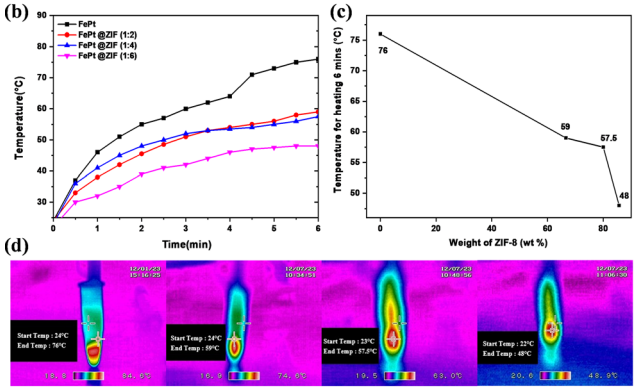

Fig. 4 Magnetic hyperthermia measurement (MFH) results and analysis. (a) $\Delta T/\Delta t$ and SAR of FePt and FePt/ZIF-8 nanocomposite materials. (b) Magnetic heating curves of FePt and FePt@ZIF nanocomposite materials. (c) Temperature of FePt@ZIF nanocomposite materials after 6 minutes of heating. (d) Thermal imaging of FePt@ZIF nanocomposite materials.

In this equation, $\Delta T/\Delta t$ represents the relationship between temperature change and time, C is the weight-weighted average of the specific heat capacity of the magnetic nanoparticles and water, and m_{FePt} refers to the weight of the magnetic nanoparticles. The unit is expressed as the heating power per unit weight (W g^{-1}). Following this, tumor-bearing mice were also injected with the magnetic samples, and AMF was used to treat their body temperature changes, as shown in Fig. S3a. The temperature changes before and after sample injection were recorded, as shown in Fig. S3b. It was observed that, except for the pure ZIF-8 group, tumor temperatures increased after sample injection. Among them, the pure FePt group exhibited the highest temperature increase, which was consistent with the saturation magnetization results (Fig. S3c), indicating that even after heating ceased, the tumor environment retained a good heating effect (Fig. S4). Evaluating nanoparticles for use in biological environments is fundamental to ensuring their safety, efficacy, and reliability for medical applications, diagnostics, and beyond. To begin the analysis, we conducted fundamental bioactivity tests on the material. To evaluate the biocompatibility of FePt@ZIF nanocomposites for biomedical applications, cytotoxicity was measured using human liver cancer cell lines (SK-HEP-1 and Mahlavu) exposed to FePt and FePt@ZIF at varying concentrations for 48 hours, as shown in Fig. S5a and S5b. The results indicated that FePt and FePt@ZIF nanocomposites did not reduce cell viability in cancer cells, with cell survival rates consistently above 90%. This demonstrates that FePt and FePt@ZIF nanocomposites possess excellent biocompatibility. We used laser scanning confocal microscopy to compare phagocytosis between FePt@ZIF and FePt@ZIF-m to assess nanoparticle uptake. Guided by an external magnetic field, we investigated whether FePt@ZIF-m could quickly accumulate inside cells to enhance future MRI contrast imaging. Confocal microscopy images revealed that, under magnetic guidance, FePt@ZIF-m coated with the red blood cell membrane demonstrated superior accumulation inside cells, as shown in Fig. S5c. These results illustrate that FePt@ZIF-m has excellent biological properties and may greatly facilitate subsequent MRI detection. In addition to conducting *in vitro* bioactivity assays on cell lines, we also established a mouse orthotopic HCC model to simulate the subsequent integration of FePt@ZIF-m as an *in vivo* biosensing module for future work. Based on previous research, high concentrations of nanomaterials, over 2 mg in the whole body of mice, will block blood vessels and cause serious harm to mice.

To avoid this, we tried to use the RBC-m structure to improve iron-based nanoparticles such as FePt@ZIF-m so that the nanoplatform can deliver clearer and simpler MRI imaging results with fewer materials. The *T*1-weighted and *T*2-weighted MRI scans (as shown in Fig. 5a) demonstrated that FePt@ZIF-m nanomaterials create a strong contrast between healthy liver tissue and liver cancer (HCC), clearly showing the tumor's location. This suggests that FePt@ZIF-ms are suitable for use as

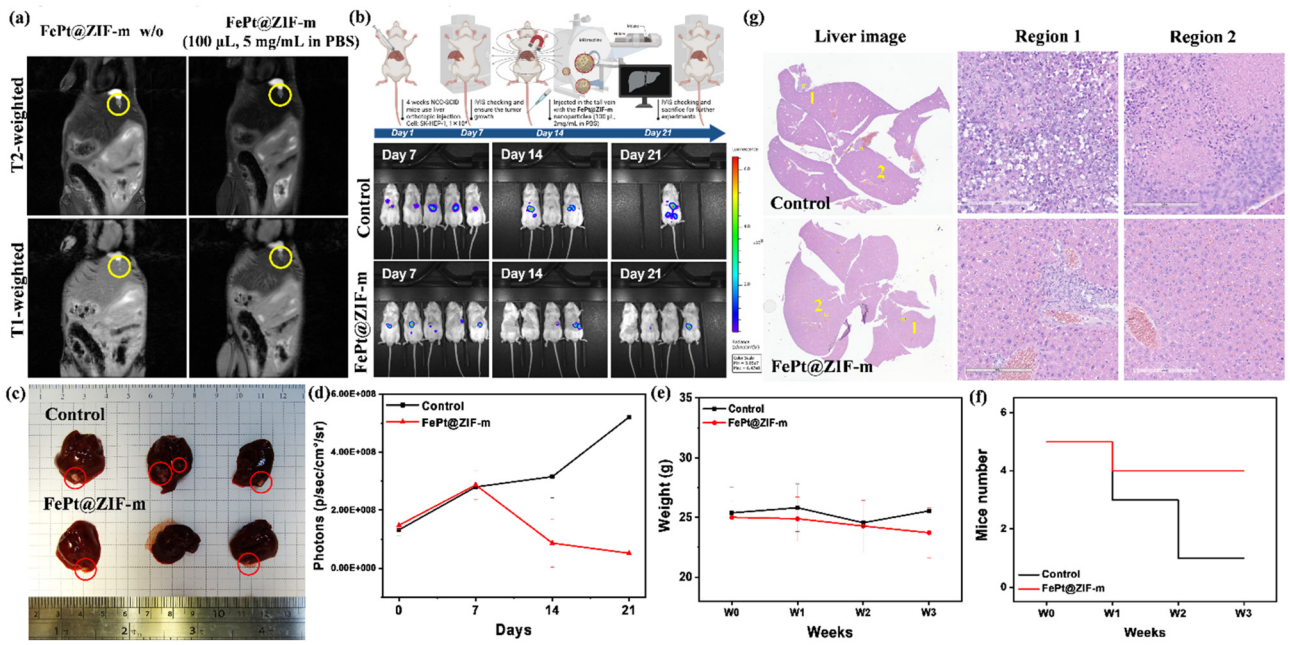

Fig. 5 Mouse HCC orthotopic tumor cell model and diagnostic and therapeutic evaluation. (a) *T*1-weighted/*T*2-weighted MRI imaging showing pre- and post-FePt@ZIF-m nanoparticle injection for mice liver diagnosis. (b) Workflow of the *in vivo* experiment and IVIS imaging reveals the tumor growth of the SK-HEP-1 orthotopic model and region for the mice's liver, and the data can be quantified to measure the tumor size of the mice each week through the absolute photon number (n = 5). (c) Images of the liver after the sacrifice of mice. The mice and tumor evaluation curve of (d) IVIS quantification, (e) mice weight, and (f) Kaplan–Meier survival curve. (g) H&E staining with liver tissue (scale bar = 200 μm), circled with two regions.

contrast agents in imaging. Moreover, we tracked how liver tumors grew using MRI and another quick imaging method called Xenogen IVIS Spectrum Noninvasive Quantitative Molecular Imaging System (IVIS). While IVIS is not as precise as MRI in showing the tumor's size and location, it still provides quick, measurable data for assessing tumor growth. In untreated mice, the tumors grew rapidly; thus, we could detect changes in tumors within two weeks (Fig. 5b). Next, the mice were injected intravenously (IV) with FePt@ZIF-m (100 μL, 5 mg mL^{-1} in PBS) and subjected to MRI imaging and MFH treatment in an attempt to inhibit cancer cell growth. The IVIS results from each week indicated a significant inhibitory effect on cancer cell growth, showing a clear difference compared to the control group that received only PBS. However, since only one mouse in the control group survived after 28 days, it was difficult to statistically calculate a reliable confidence interval. The mice were sacrificed, and images were obtained through photography. Since some mice died prematurely, certain organ images were taken from the liver of mice on day 14 (two control group mice, Fig. 5c). Additionally, IVIS images were further analyzed quantitatively to measure fluorescence intensity (Fig. 5d). The physiological conditions of the mice were evaluated using body weight and survival curves, as shown in Fig. 5e and f, respectively. There was no significant difference in body weight before and after treatment; however, survival rates were significantly improved, effectively extending the lifespan of the treated mice compared to the control group. H&E staining was performed on the liver tissues of the mice, revealing tumor tissue growth in different regions. After FePt@ZIF-m treatment, tumor size was noticeably reduced, and histological sections exhibited hollow tissue structures, suggesting that the MFH effect induced by heat contributed to cancer cell inhibition (Fig. 5g).

Conclusions

ZIF-8 (zeolitic imidazolate framework-8) was first synthesized using a one-pot method, while FePt nanoparticles were prepared *via* a chemical reduction method.[45] Subsequently, FePt nanoparticles were composited with ZIF-8 using a vacuum-assisted assembly process, adjusting the ZIF-8 ratio to obtain FePt@ZIF nanocomposites with different properties. Finally, red blood cell membranes were physically coated onto the composites to fabricate FePt@ZIF-m nanocomposites. These materials were then analyzed for their crystal structure, microstructure, surface properties, magnetic characteristics, biocompatibility, thermal stability, MRI contrast efficiency, and magnetic hyperthermia (MFH) effects. Increasing the proportion of ZIF-8 reduced the saturation magnetization of the nanocomposites. The SAR (specific absorption rate) value decreased from 97.67 W g^{-1} to 44.19 W g^{-1}, yet all samples could still reach 42 °C within 3 minutes, a temperature sufficient to kill cancer cells. *In vivo* studies demonstrated that the injected FePt@ZIF composites retained heating effects in mice. The FePt@ZIF nanocomposites demonstrated excellent magnetic properties, drug-loading capabilities, and biocompatibility. These materials hold promise for applications in MFH therapy, MRI contrast agents, and targeted drug delivery, offering a multifunctional approach for cancer treatment.

Experimental section

Preparation of superparamagnetic FePt nanoparticles

Iron acetylacetonate (0.45 mmol, 0.1589 g) and platinum acetylacetonate (0.3 mmol) were weighed using a microbalance and dissolved in 30 mL of tetraethylene glycol (TEG) in a three-necked flask with a magnetic stir bar. The setup was assembled, the condenser was covered with a balloon to prevent gas leakage, and 1 mL of silicon oil was placed in the temperature probe tube for accurate heat transfer. The flask was purged with argon for 10 minutes to create an inert atmosphere and cooling water was circulated through the condenser. The solution was heated at 5 °C min^{-1} to 200 °C, and then the argon flow was stopped and the temperature was maintained for 1 hour. 1 mL of oleic acid was added, the temperature was maintained at 200 °C for 30 minutes, and then it was heated at 5 °C min^{-1} to 300 °C, where it was held for another hour. The color change from reddish-brown to metallic gray confirmed FePt NP formation.

Preparation of ZIF-8

1.2 g each of zinc nitrate hexahydrate ($Zn(NO_3)_2{\cdot}6H_2O$) and 2-methylimidazole were weighed using a microbalance and then dissolved in 30 mL of methanol in a 50 mL three-necked flask with a magnetic stir bar. The mixture was stirred at 80 rpm for 1 hour and was left to stand at room temperature for 24 hours. The precipitate was collected, washed with ethanol, and centrifuged at 6000 rpm for 15 minutes, and this process was repeated four times. The purified sample was dried in an oven to obtain ZIF-8 as a white powder.

Preparation of the FePt@ZIF nanocomposite material

FePt NPs were dispersed in ethanol and sonicated for 30 minutes. Varying amounts of ZIF-8 were added to the dispersion and then sonicated for another 30 minutes. The tube was placed in a vacuum bag and subjected to vacuum for 30 minutes before allowing it to break naturally. The particles were purified by adding ethanol and centrifuging at 6000 rpm for 10 minutes. The purified particles were dried in an oven to obtain the grayish-white FePt@ZIF nanocomposite powder.

Preparation of FePt@ZIF-a nanocomposite material

DNA/RNA aptamers with high affinity for ZIF-8 were selected or designed, using 100 ng mL^{-1} sequences targeting Zn or imidazole groups. The aptamers' 5′ or 3′ ends were modified with functional groups (*e.g.*, amines) for conjugation and a PEG linker was added for flexibility. The ZIF-8 surface was activated with EDC/NHS for carboxyl-amine coupling with the aptamers. The ZIF-aptamer conjugates were washed thoroughly to remove unbound aptamers and then FePt NPs were loaded into the pores using vacuum decompression.

Preparation of the FePt@ZIF-m nanocomposite material

Mouse whole blood was centrifuged at 3000 rpm for 10 minutes to separate plasma, platelets, RBCs, and white blood cells. All components were removed except RBCs, washed once with PBS, and mixed with 0.5 M EDTA at a 1 : 50 ratio. This was left to stand on ice for 15 minutes and then centrifuged at 700*g* for 5 minutes to remove white blood cells. The supernatant was centrifuged at 14 000 rpm for 20 minutes at 4 °C. The supernatant was filtered through an 800 nm membrane into a tube, repeating 15 times to obtain RBC-m. The FePt@ZIF nanocomposite was mixed with RBC-m (1 mg mL^{-1}), filtered through the membrane 15 times, and the FePt@ZIF-m nanocomposite was stored at 4 °C.

Cell culture and stable clone establishment

Dulbecco's modified Eagle's medium (DMEM) and minimum essential medium (MEM) supplemented with 10% FBS (Invitrogen, Carlsbad, CA, USA) were used to grow human HCC cell lines, SK-HEP-1 and Mahlavu. We set all cells at 37 °C in a humidified atmosphere of 5% CO_2. The ATCC cell bank was used to acquire the cell lines.

Magnetic hyperthermia performance

To further augment the therapeutic efficacy of FePt@ZIF-m, we explored its potential for magnetic hyperthermia (MFH) under an alternating magnetic field (AMF). The embedded FePt nanocrystals within the MOF framework exhibited efficient magnetic-to-thermal energy conversion due to their high magnetic susceptibility and nanoscale confinement. Upon AMF exposure (f = 500 kHz, H = 30 kA m^{-1}), a rapid temperature elevation was observed at a concentration of 6 mg mL^{-1}. The specific absorption rate (SAR) was calculated to confirm the MFH capability of the hybrid construct.

Animal tumorigenicity study

JAX®, NOD-SCID* mice (4–6 weeks old, 20–25 g body weight) that were non-obese, diabetic, and severely combined immune-deficient gamma (NOD.Cg-Prkdcscid Il2rgtm1Wjl/SzJ) were used. To test lung cancer cell tumorigenicity, severely diluted 1E102–4 cells were resuspended in 100 μL of PBS and injected subcutaneously or orthotopically into the flank regions. An IVIS system was used to determine the tumor size by measuring each tumor's length (L) and width (W) and calculating the tumor volume as $1/2 \times LW^2$. The National Yang Ming Chiao Tung University Institutional Animal Care and Utilization Committee (IACUC) approved all animal experiments conducted on animals.

Pathological tissue fluorescence analysis

Tumor samples from mice were fixed with 10% formalin and antigen retrieval was performed by heating slides in a 100 mM Tris, 5% urea buffer (pH 9.5) at 95 °C for 10 minutes. The slides were washed with PBS three times. The cells were permeabilized with PBS containing 0.2% Triton X-100 for 15 minutes. Blocking buffer (1% BSA, 1% FBS, 22.52 mg mL^{-1} glycine in PBST) and 5 mg mL^{-1} DAPI (1 : 1000 dilution in blocking buffer) were prepared. The cells were incubated in blocking buffer for 1 hour and then stained with primary antibodies (human CD47 and FePt@ZIF-m, 1 : 150 dilution) in blocking buffer overnight at 4 °C. 20–30 ng μL^{-1} mounting solution was added to cover the slides.

Statistical analysis

Data are shown as means ± SD, with $n \geq 3$, and significance was tested using ANOVA or two-tailed Student's t-test as appropriate, with light intensity as means ± SE. Statistical annotations have been added to all relevant figures. Kaplan–Meier and Cox regression analyses were used to assess survival, with two-sided tests and significance set at $P < 0.05$.

Author contributions

Ming-Hsien Chan: conceptualization, investigation, writing – original draft, writing – review & editing, and funding acquisition; Ru-En Zhuang: investigation, methodology, and visualization; Da-Hua Wei: resources, supervision, and project administration; Michael Hsiao: supervision, validation, writing – review & editing, and project administration.

Conflicts of interest

There are no conflicts to declare.

Data availability

Electronic supplementary information (ESI) available: SEM/EDX mapping; BET surface-area and TGA/DTA analyses; thermal imaging; *in-vitro* biocompatibility assays and confocal microscopy. The data supporting this article have been included as part of the SI. See DOI: **https://doi.org/10.1039/d5nr03294f**.

Acknowledgements

This work has received funding from the National Science and Technology Council (NSTC) through grants numbered 112-2113-M-A49-037-MY2 and 114-2113-M-A49-031-MY3 to M. H. C. and 112-2740-M-027-001 and 112-2221-E-027-111 to D. H. W. The Yen Tjing Ling Medical Foundation (project number: CI-113-4) is gratefully acknowledged for financial support. We thank the GRC Instrument Core Facilities for granting high-performance confocal and flow cytometry measurements.

References

1 S. Chidambaranathan-Reghupaty, P. B. Fisher and D. Sarkar, *Adv. Cancer Res.*, 2021, **149**, 1–61.

2 J. X. Huang, W. H. Zhang, Y. M. Wu, J. Y. Hu, H. Long, H. D. Zhu, J. Q. Zhang, G. J. Teng and F. Xiong, *Adv. Healthcare Mater.*, 2024, **13**, e2402253.
3 D. Zhang, C. W. Jiang, X. Y. Zheng, Z. W. Lin, Q. Y. Zhuang, H. Z. Xie, Y. Z. Liang, Y. Xu, L. S. Cui, X. L. Liu and Y. Y. Zeng, *Small*, 2023, **19**, e2207786.
4 X. Liu, X. Lin, M. Wu, R. Lin, B. Li and J. Liu, *J. Mater. Chem. B*, 2016, **4**, 4119–4129.
5 M. O. Besenhard, L. Panariello, C. Kiefer, A. P. LaGrow, L. Storozhuk, F. Perton, S. Begin, D. Mertz, N. T. K. Thanh and A. Gavriilidis, *Nanoscale*, 2021, **13**, 8795–8805.
6 X. Zhao, X. Sun, W. Huang, R. Chen, K. Chen, L. Nie and C. Fang, *J. Nanobiotechnol.*, 2022, **20**, 100.
7 M. H. Chan, C. H. Li, Y. C. Chang and M. Hsiao, *Pharmaceutics*, 2022, **14**, 1282.
8 R. S. Gomes, R. P. das Neves, L. Cochlin, A. Lima, R. Carvalho, P. Korpisalo, G. Dragneva, M. Turunen, T. Liimatainen, K. Clarke, S. Yla-Herttuala, C. Carr and L. Ferreira, *ACS Nano*, 2013, **7**, 3362–3372.
9 S. Lopez, N. Hallali, Y. Lalatonne, A. Hillion, J. C. Antunes, N. Serhan, P. Clerc, D. Fourmy, L. Motte, J. Carrey and V. Gigoux, *Nanoscale Adv.*, 2022, **4**, 421–436.
10 H. Hamza, A. M. Ferretti, C. Innocenti, K. Fidecka, E. Licandro, C. Sangregorio and D. Maggioni, *Inorg. Chem.*, 2020, **59**, 12086–12096.
11 D. H. Wei and Y. D. Yao, *J. Appl. Phys.*, 2011, **109**, 07E302.
12 J. Kim, Y. Lee and S. H. Sun, *J. Am. Chem. Soc.*, 2010, **132**, 4996–4997.
13 K. X. Yu, Y. Chen, L. Zhang, Y. Q. Zheng, J. L. Chen, Z. H. Wang, X. G. Yu, K. H. Song, Y. M. Dong, F. X. Xiong, Z. J. Dong, H. Zhu, G. H. Sheng, M. P. Zhu, X. Yuan, H. F. Guan, J. Q. Xiong, Y. Liu and F. Li, *ACS Appl. Mater. Interfaces*, 2023, **15**, 44689–44710.
14 H. Arami, A. Khandhar, D. Liggitt and K. M. Krishnan, *Chem. Soc. Rev.*, 2015, **44**, 8576–8607.
15 L. H. Reddy, J. L. Arias, J. Nicolas and P. Couvreur, *Chem. Rev.*, 2012, **112**, 5818–5878.
16 C. Sun, J. S. H. Lee and M. Q. Zhang, *Adv. Drug Delivery Rev.*, 2008, **60**, 1252–1265.
17 Z. F. Hu, Q. L. Wei, H. M. Zhang, W. N. Tang, Y. K. Kou, Y. Q. Sun, Z. C. Dai and X. W. Zheng, *J. Mater. Chem. B*, 2022, **10**, 339–357.
18 M. X. Wu and Y. W. Yang, *Adv. Mater.*, 2017, **29**, 1606134.
19 H. Bunzen and D. Jirak, *ACS Appl. Mater. Interfaces*, 2022, **14**, 50445–50462.
20 L. L. Sun, Z. J. Xiong, F. Y. Shen, Z. H. Wang and Z. Liu, *Sci. China: Chem.*, 2021, **64**, 719–733.
21 W. S. Seo, J. H. Lee, X. M. Sun, Y. Suzuki, D. Mann, Z. Liu, M. Terashima, P. C. Yang, M. V. McConnell, D. G. Nishimura and H. J. Dai, *Nat. Mater.*, 2006, **5**, 971–976.
22 C. L. G. Harman, N. Mac Fhionnlaoich, A. M. King, J. R. H. Manning, W. Lin, P. Scholes, S. Guldin and G.-L. Davies, *Mater. Adv.*, 2022, **3**, 6007–6018.
23 L. Zhang, Z. Q. Cao, T. Bai, L. Carr, J. R. Ella-Menye, C. Irvin, B. D. Ratner and S. Y. Jiang, *Nat. Biotechnol.*, 2013, **31**, 553–556.
24 C. Moya, R. Escudero, D. C. Malaspina, M. de la Mata, J. Hernández-Saz, J. Faraudo and A. Roig, *ACS Appl. Bio Mater.*, 2019, **2**, 3084–3094.
25 P. Guardia, R. Di Corato, L. Lartigue, C. Wilhelm, A. Espinosa, M. Garcia-Hernandez, F. Gazeau, L. Manna and T. Pellegrino, *ACS Nano*, 2012, **6**, 3080–3091.
26 M. Shokouhimehr, E. S. Soehnlen, J. H. Hao, M. Griswold, C. Flask, X. D. Fan, J. P. Basilion, S. Basu and S. P. D. Huang, *J. Mater. Chem.*, 2010, **20**, 5251–5259.
27 D. H. Wei, K. Y. Pan and S. K. Tong, *Materials*, 2017, **10**, 181.
28 P. H. D. Nguyen, M. K. Jayasinghe, A. H. Le, B. Y. Peng and M. T. N. Le, *ACS Nano*, 2023, **17**, 5187–5210.
29 P. Railey, Y. Song, T. Y. Liu and Y. Li, *Mater. Res. Bull.*, 2017, **96**, 385–394.
30 L. Zhu, Y. Li, J. Zhao, J. Liu, L. Wang, J. Lei and R. Xue, *Chem. Commun.*, 2022, **58**, 2906–2909.
31 W. T. Shi, L. Bian, Y. Q. Wu, Z. Wang, Y. Dai, Y. J. Zhou, P. F. Meng, Q. Wang, Z. J. Zhang, X. J. Zhao, P. Zhao and X. J. Lu, *Macromol. Biosci.*, 2022, **22**, 113015.
32 L. Sun, W. Jiang, H. Zhang, Y. Guo, W. Chen, Y. Jin, H. Chen, K. Du, H. Dai, J. Ji and B. Wang, *ACS Appl. Mater. Interfaces*, 2019, **11**, 2302–2316.
33 M. R. Ahmadian-Yazdi, N. Gholampour and M. Eslamian, *ACS Appl. Energy Mater.*, 2020, **3**, 3134–3143.
34 R. Tahmasebpour and S. J. Peighambardoust, *Sep. Purif. Technol.*, 2024, **343**, 127188.
35 R. Ettlinger, S. M. Vornholt, M. C. Roach, R. R. Tuttle, J. Thai, M. Kothari, M. Boese, A. Holwell, M. J. Duncan, M. Reynolds and R. E. Morris, *ACS Appl. Mater. Interfaces*, 2023, **15**, 49835–49842.
36 Z. Latrach, E. Moumen, S. Kounbach and S. El Hankari, *ACS Omega*, 2022, **7**, 15862–15869.
37 J. Yu, F. Chen, W. L. Gao, Y. M. Ju, X. Chu, S. L. Che, F. G. Sheng and Y. L. Hou, *Nanoscale Horiz.*, 2017, **2**, 81–88.
38 Q. F. Chen, X. B. Ma, L. Xie, W. J. Chen, Z. G. Xu, E. Q. Song, X. K. Zhu and Y. Song, *Nanoscale*, 2021, **13**, 4855–4870.
39 S. Chung, R. A. Revia and M. Q. Zhang, *Nanoscale Horiz.*, 2021, **6**, 696–717.
40 K. H. Hong, W. C. Elias, K. N. Heck, T. Terlier, D. Dimpel, W. Qian, B. Liu, T. Kurihara and M. S. Wong, *Catal. Today*, 2025, **453**, 115254.
41 J. Xiao, J. Weng, F. Wen and J. Ye, *ACS Omega*, 2020, **5**, 32861–32867.
42 M. F. Murphy, S. Rajbhandary, S. Carayiannis and C. S. Cohn, *Transfusion*, 2024, **64**, 1217–1222.
43 X. W. Yang, M. C. Chen, C. Y. Weng, D. L. Zhuge, F. S. Jin, Y. N. Xiao, D. Y. Tian, Q. Q. Yin, L. Li, X. F. Zhang, G. H. Shi, X. S. Lu, L. Z. Yan, L. D. Wang, B. Wen, Y. Z. Zhao, J. J. Lin, F. Wang, W. X. Zhang and Y. J. Chen, *Adv. Sci.*, 2024, **11**, e2310230.
44 J. H. Lin, K. Y. Pan, D. H. Wei and R. J. Chung, *Surf. Coat. Technol.*, 2018, **350**, 868–873.
45 H. Yang, J. J. Zhang, Q. W. Tian, H. Hu, Y. Fang, H. X. Wu and S. P. Yang, *J. Magn. Magn. Mater.*, 2010, **322**, 973–977.